analytical chemistry

pubs.acs.org/ac

Article

Magnetofluid-Integrated Multicolor Immunochip for Visual Analysis of Neutralizing Antibodies to SARS-CoV-2 Variants

Haicong Shen, Xinying Chen, Liuqing Zeng, Xing Xu, Yingzhou Tao, Siyin Kang, Yinzhu Lu, Mingjian Lian, Chaoyong Yang, and Zhi Zhu*

Cite This: *Anal. Chem.* 2022, 94, 8458–8465

Read Online

ACCESS | Metrics & More | Article Recommendations | Supporting Information

ABSTRACT: The global spread of SARS-CoV-2 virus has severely affected human health, life, and work. Vaccine immunization is considered to be an effective means to protect the body from infection. Therefore, timely analysis of the antibody level is helpful to identify people with low immune response or attenuated antibodies so as to carry out targeted and precise vaccine booster immunization. Herein, we develop a magnetofluid-integrated multicolor immunochip, as a sample-to-answer system in a fully enclosed space, for visual analysis of neutralizing antibodies of SARS-CoV-2. Generally, this chip adopts an innovative three-dimensional two-phase system that utilizes mineral oil to block the connection between reagent wells in the vertical direction and provides a wide interface for rapid and nondestructive shuttle of magnetic beads during the immunoassay. In order to obtain visualized signal output, gold nanorods with a size-dependent color effect are used as the colorful chromogenic substrates for evaluation of the antibody level. Using this chip, the neutralizing antibodies were successfully detected in vaccine-immunized volunteers with 83.3% sensitivity and 100% specificity. Furthermore, changes in antibody levels of the same individual over time were also reflected by the multicolor assay. Overall, benefiting from simple operation, airtight safety, and nonrequirement of external equipment, this platform can provide a new point-of-care testing strategy for alleviating the shortage of medical resources and promoting epidemic control in underdeveloped areas.

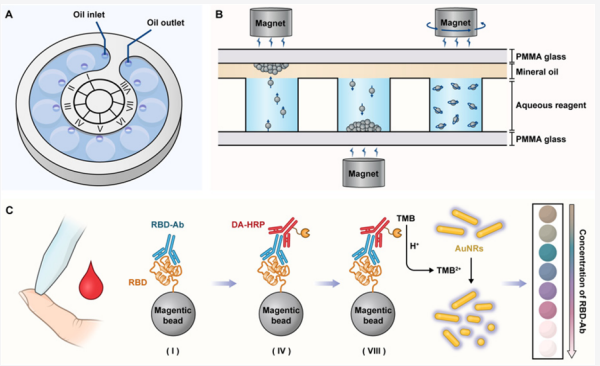

Corona Virus Disease 2019 (COVID-19) is a severe, acute respiratory infectious disease caused by the SARS-CoV-2 virus.[1] Currently, the global spread of the disease has caused hundreds of millions of infections, including over five million deaths. Universal vaccination seems to be the most useful means to control the epidemic of the virus and limit the morbidity and mortality. This goal has benefited mainly from the protection effect of short-term neutralizing antibodies (NAbs) and long-term immune memory ability.[2] It is worth noting that age or underlying diseases can cause differences in the NAbs levels between immunized individuals, and the NAbs level of the same individual may decrease over time.[3] Although many people were fully vaccinated, some have still been infected with COVID-19. Therefore, quantitative or semi-quantitative analysis of NAbs after immunization is of great significance to evaluate the effectiveness of vaccines. Such data will also provide information about individuals with low immune responses or weakened antibodies, leading to protective measures such as strengthening immunity.[4]

SARS-CoV-2 virus contains four structural proteins: the nucleocapsid (N), membrane (M), envelope (E), and spike (S) proteins. Notably, the entry of virus particles into host cells is mainly achieved by the interaction of S protein and specific binding of receptor (angiotensin converting enzyme-2, ACE2) and membrane fusion.[5] Therefore, blocking the recognition of the receptor binding domain (RBD) on S protein to ACE2 by NAbs is an effective means to prevent viral infection. Actually, only a subset of antibodies of RBD shows neutralization function. Ju et al. reported that 7 of 16 RBD binding antibodies neutralized a live SARS-CoV-2.[6] Compared with other regions with neutralizing effect (such as N-terminal domain, fusion peptide), RBD induces the majority of neutralizing activity.[7,8] Therefore, for convenience, we considered the RBD binding antibodies as neutralizing antibodies (NAbs). Neutralization assay based on viral plaque counts is the gold standard for the assessment of NAbs, but it involves time-consuming and laborious procedures and requires advanced laboratory facilities.[9]

As an alternative strategy, the concentration of NAbs against RBD can be used as indicators of the immunity level.[10,11]

Received: March 22, 2022
Accepted: May 20, 2022
Published: June 3, 2022

https://doi.org/10.1021/acs.analchem.2c01260
Anal. Chem. 2022, 94, 8458–8465

Traditional laboratory analyses (such as ELISA) with high accuracy and throughput are very suitable for monitoring the NAb level of a large number of samples in a modern laboratory setting.[12] ELISA also requires specialized and time-consuming procedures, which makes it difficult to apply to point-of-care diagnosis. Fluorescent microsphere immunoassays have also been established for the rapid detection of SARS-CoV-2 antibodies. However, it is currently designed for laboratory use only as they require fluorescent collection devices.[13] As an alternative POCT platform, lateral flow immunoassays have the advantages of simplicity and speed in the analysis of SARS-CoV-2 antibodies, which is limited by the qualitative analysis.[14] Generally, the corresponding POCT platform should preferably have the features of quantitative or semi-quantitative detection ability, visual signal output, integrated operation, airtight safety, and nonrequirement of external equipment.

As a total analysis system, microfluidic technology has unique advantages in terms of precise fluid control, reagent transfer and mixing, and system automation, which has good prospects in POCT.[15−20] For instance, Qin's group developed an integrative volumetric bar-chart chip for quantitative immune-analysis.[21] The chip realizes step-by-step reactions and visual output of air pressure signals by movement of different slices of the chip. Although this design cleverly realizes integrated detection, the strict air-tightness requirements between the chip slices cause certain difficulties for reagent addition, transfer, and signal output. Zeng's group used an elastic polymer (polydimethylsiloxane, PDMS) to prepare a pneumatically gated microfluidic chip for integrated magnetic fluid immunoassay.[22] In their work, a precise gas valve allows the immunomagnetic beads to participate in a multistep reaction in a closed chip and directly produces the final fluorescence signal. However, it is more suitable for microvolume reactions due to the high demands in air pump control and micro-nano fabrication. To automate operations, Tian et al. developed a fully automated centrifugal microfluidic system for sample-to-answer viral nucleic acid testing.[23] This work has the advantages of automation and multiplex detection but requires a specialized centrifugal device. In order to achieve simple chip preparation and operation, researchers developed an equipment-free microfluidic plastic chip with a water−oil two-phase system for bioanalysis.[24,25] Although the horizontal staggered arrangement of oil−water phases can effectively integrate multistep reactions, the design still has several shortcomings. First, in order to form a stable oil−water arrangement, the connecting channel between the oil and water phases should be as small as possible, which causes difficulties in the shuttle of the magnetic beads. Second, the volume of water or oil is constant, which makes it difficult to meet the requirements of reagent addition or reaction heating. Therefore, the instability accompanied by the change in volume limits the wide application of this design. Finally, although the linear injection hole in the chip enhances air-tightness, it is accompanied by difficulty in adding samples and residual reagents. Recently, Juang et al. developed an oil-immersed lossless total analysis system for the detection of SARS-CoV-2 virus.[18] In this study, they constructed discrete hydrophilic sites on the chip surface to load microdroplets. The enrichment, amplification, and analysis of RNA was realized by the shuttle of magnetic beads in the peripheral oil phase. However, it is still limited by a fixed solution volume and cannot realize the addition of reagents.

To overcome the above problems, we developed a novel magnetofluid-integrated multicolor immunochip (MMI-Chip) for visual analysis of NAbs to SARS-CoV-2 variants. The MMI-Chip uses mineral oil to block the connection between reagent wells in the vertical direction, and provides a wide interface for rapid and nondestructive shuttle of magnetic beads. Furthermore, since the oil phase floats above the reagent wells, the volume change caused by reagent addition, mixing, and heating can be balanced by adjusting the oil phase. Additionally, the newly designed circular injection hole can realize nondestructive addition and mixing of reagents as well as one-time oil sealing, which greatly saves the operating time. During the experiment, the MMI-Chip performs integrated and airtight reactions by immunomagnetic fluid based on the shuttle of magnetic beads between mineral oil and reagents by the movement of a magnet. In order to obtain visualized signal output, gold nanorods (AuNRs) with a size-dependent color effect are utilized as the ideal chromogenic substrates.[26,27] Generally, horseradish peroxidase (HRP) combined with HCl can oxidize tetramethylbenzidine (TMB) to the divalent state, and then it etches the AuNRs to generate different colors. We believe the MMI-Chip can provide a new strategy for individualized antibody assessment and efficient epidemic control.

EXPERIMENTAL SECTION

Reagents and Materials. Hexadecyl trimethyl ammonium bromide (CTAB), sodium borohydride ($NaBH_4$), chloroauric acid ($HAuCl{\cdot}4H_2O$), silver nitrate ($AgNO_3$), and ascorbic acid, were provided by Sinopharm Chemical Reagent Co., Ltd. (Shanghai, China). SARS-CoV-2 (2019-nCoV) spike protein (RBD, His Tag), SARS-CoV-2 (2019-nCoV) spike neutralizing antibody, and rabbit Mab (A18805), were provided by Sinobiological Co., Ltd. (Beijing, China). Goat anti-human IgG-HRP was purchased from Thermo Fisher Scientific (Waltham, MA, USA). Goat anti-rabbit-HRP was provided by the R&D System (Minneapolis, MN, USA). Ni-Charged MagBeads were provided by Genscript Co., Ltd. (Piscataway, NJ, USA). Soluble TMB substrate solution (A + B) was purchased from Tiangen Biotech Co., Ltd. (Beijing, China). Mineral oil (light) was provided by Sigma-Aldrich (St. Louis, MO, USA). Nonfat-dried milk, phosphate buffered saline (PBS), and Tween-20 were obtained from Sangon Biotech Co. Ltd. (Shanghai, China). The laser-cutting machine was purchased from Dongguan Foreverqi Mechanical Equipment Co. Ltd. (Dongguan, China). Transmission electron microscope 2100 (TEM) was purchased from JEOL (Beijing, China). The microplate reader was purchased from Molecular Devices (Silicon Valley, CA, USA).

Preparation of the MMI-Chip. The chip was designed using the Auto-CAD software, and then different powers of the laser-cutting machine were used for cutting PMMA of different thickness. As shown in Figure S1, the cutting power required for PMMA with a thickness of 3 mm (red), 1 mm (green), and 0.2 mm (blue) is 100, 50, and 10 mW, respectively. Finally, the PMMA layers can be assembled after cleaning with distilled water, soaking in PBST (containing 5% milk), and drying. The assembly of the chip was completed by using the adhesive force of transparent double-sided tape.

Preparation of Gold Nanorods. The synthesis of AuNRs with controllable size was achieved according to the seed growth method.[27] First, the seed solution was prepared. CTAB (0.2 M, 5 mL) and $HAuCl_4$ (0.5 mM, 5 mL) were added into a 20 mL glass bottle and mixed at 500 rpm. At this time, the solution was golden yellow. Then, the speed was adjusted to 1200 rpm, and chilled $NaBH_4$ (0.01 M, 0.6 mL) was quickly added. After 2 min

https://doi.org/10.1021/acs.analchem.2c01260
Anal. Chem. 2022, 94, 8458−8465

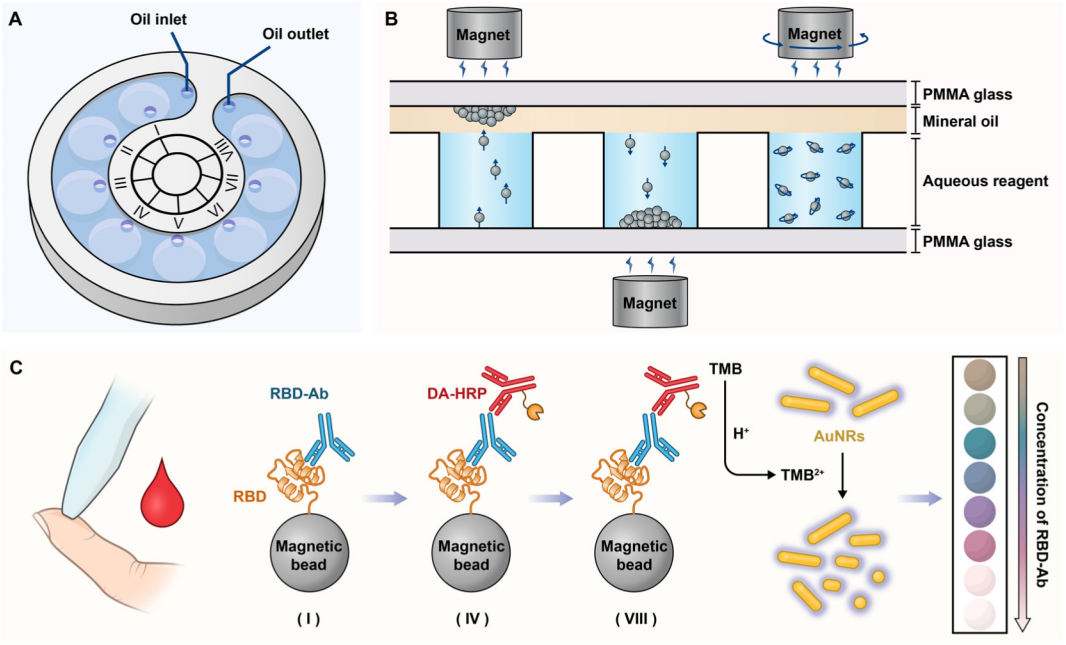

Figure 1. Schematic illustration of the MMI-Chip. (A) Structural diagram of the chip. It contains eight liquid wells for loading sample (I), washing solution (II, III), detection antibody (IV), washing solution (V–VII), and signal substrate (VII). (B) The process of magnetic beads shuttling between the reagents and the mineral oil. Through the vertical and horizontal movement of the magnet, the magnetic beads can pass through the oil phase to participate in different reactions. Mixing of the solution is achieved by the rotation of the magnet. (C) Workflow of detection of NAbs. Magnetic beads immobilized with RBD (MBs-RBD) successively complete the capture of target antibody (RBD-Ab) derived from peripheral blood, binding of detection antibody (DA-HRP), and reaction with substrate (TMB). Finally, HCl and AuNRs are added to reservoir VII to obtain the antibody concentration-dependent multicolor signal.

of stirring, the solution turned from golden yellow to brown. Next, the solution was kept at 30 °C for 10 min and stored at room temperature for later use. Second, the growth solution was prepared. $AgNO_3$ (0.01 M, 0.60 mL) was added to CTAB (0.1 M, 73.76 mL) in a 100 mL sample bottle and then stirred for 2 min at 700 rpm. After holding at 30 °C for 15 min, $HAuCl_4$ (10 mM, 4 mL) was added and mixed at 1200 rpm for 2 min. Then, ascorbic acid (0.01 M, 4.4 mL) was added dropwise, and the solution gradually became colorless. Finally, 160 μL of seed solution was added to the prepared growth solution and stirred at 1200 rpm for 20 s. After keeping in a 30 °C water bath for about 0.5 h, the λ_{max} of the AuNRs was analyzed when it was reddish-brown. If the peak was about 720 nm, the AuNRs were centrifuged and washed in a 50 mL centrifuge tube to stop the reaction (10,000 rpm, 20 min). The obtained AuNRs were resuspended in 32 mL of CTAB solution (0.1 M) and stored at room temperature. The λ_{max} and actual morphology of the AuNRs were analyzed with a microplate reader and TEM, respectively.

Preparation of Immunomagnetic Beads (MBs-RBD). After shaking and resuspending for 30 s, 200 μL of magnetic beads (25% slurry) were placed in a low-adsorption centrifuge tube. The centrifuge tube was placed on the magnetic shelf for 2 min until the beads settled. Then the supernatant was discarded. Next, 1 mL PBST was added and vortexed for 15 s to wash the magnetic beads, and the process was repeated twice. Then, 10 μg of RBD protein in 160 μL of PBST was mixed with the magnetic beads overnight at 4 °C. Then, 400 μL of PBST (containing 30% milk) was added to block the magnetic beads. Finally, the beads were resuspended in PBST (containing 0.1% proclin to prevent the growth of microorganisms).

HRP Concentration-Dependent Gold Nanorod Etching. Two microliters of DA-HRP samples with various concentrations in PBST and 100 μL of the TMB solution were placed into the wells. As a result, a series of concentrations of DA-HRP (6.7, 5.0, 4.0, 2.9, 1.3, and 0 ng mL^{-1}) were formed. After incubation away from light for 20 min, 50 μL of 1.0 M HCl was added to stop the reaction. Then, the absorbance of the solution at 450 nm (OD450) was measured. Finally, 100 μL of AuNRs solution was added to the system for 5 min for color generation. In order to further analyze the etching situation of AuNRs, the absorption spectrum of the AuNRs was also collected for calculation of λ_{max} offset.

Sensitivity and Specificity Analysis. RBD-Ab with different concentrations of 0, 10, 50, 100, 500, 1000, 1500, and 2000 ng mL^{-1} was used for sensitivity evaluation. A variety of proteins, including RBD-Ab, NP-Ab, human IgG, and rabbit IgG, were used for specificity analysis. The concentration of RBD-Ab was 500 ng mL^{-1}, while the concentrations of the other three proteins were 5000 ng mL^{-1}. In this experiment, the incubation time for RBD-Ab capture and DA-HRP binding was 25 min, while the reaction time for DA-HRP and magnetic beads was 20 min (protected from light), and the etching time of AuNRs was 5 min. In order to further analyze the etching situation of AuNRs, the absorption spectrum of the AuNRs was also collected for calculation of λ_{max} offset.

Analysis and Evaluation of Clinical Samples. Sample collection was approved by the Human Research Ethics Committee at the First Affiliated Hospital of Xiamen University (Project number: KYX-2018-006). Volunteers' blood samples were obtained by fingertip or venous blood sampling. After standing, the blood can produce a serum supernatant for further analysis. Only 2 μL of serum was required for the experiment, which can be used for antibody analysis after a 100-fold dilution. Detailed information about sample donors (10 non-vaccine-immunized volunteers and 30 vaccine-immunized volunteers) is

https://doi.org/10.1021/acs.analchem.2c01260
Anal. Chem. 2022, 94, 8458–8465

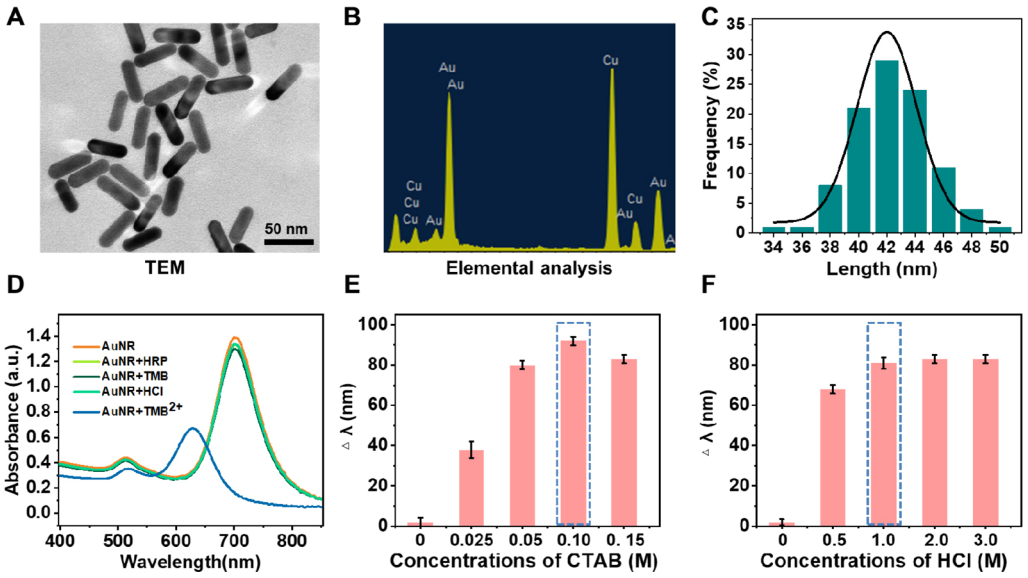

Figure 2. Characterization and etching optimization of AuNRs. (A) TEM image of AuNRs. (B) Elemental analysis of AuNRs. (C) Length distribution of AuNRs. (D) Reagent conditions for AuNR etching. (E) Optimization of CTAB concentration. Higher $\triangle\lambda$ indicates a significant shift in λ_{max} of AuNRs. (F) Optimization of HCl concentration.

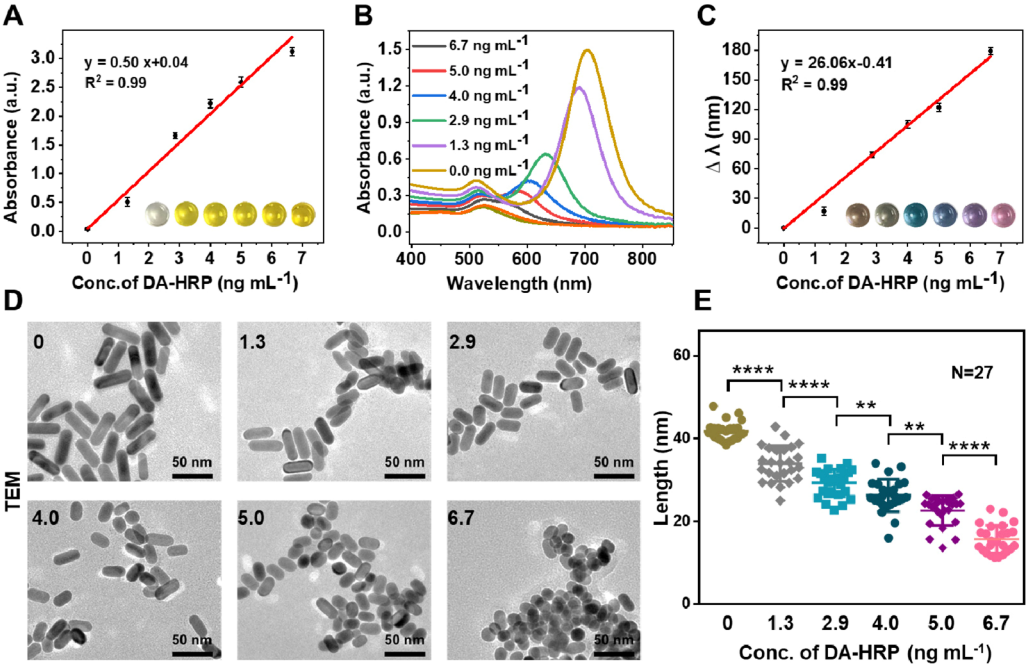

Figure 3. HRP-dependent etching of AuNRs. (A) TMB-based ELISA results under different DA-HRP concentrations. (B) Absorption spectra of AuNRs at different DA-HRP concentrations. (C) Absorption peak shift ($\triangle\lambda$) and color change of AuNRs under different DA-HRP concentrations. (D) TEM images of AuNRs at different DA-HRP concentrations. (E) Statistical length difference of AuNRs under different etching conditions.

listed in Table S1. Antibody concentrations were evaluated semi-quantitatively by the color of the AuNRs, and the clinical sensitivity and specificity of the method were calculated according to Table S3.[28]

RESULTS AND DISCUSSION

Principle and Fabrication of the MMI-Chip. The MMI-Chip contains eight liquid storage wells for loading different reagents and a double-ended closed ring structure for loading mineral oil to block the connection between reagent wells (Figure 1A). By shuttling immunomagnetic beads between mineral oil and reagents via the vertical and horizontal movement of the magnet, different reactions can be realized in distinct wells (Figure 1B). In order to perform immunoassay of neutralizing antibody, magnetic beads modified with SARS-CoV-2 Spike RBD protein (MBs-RBD) were added to the sample well. Then, multiple immunoassay steps, including capture of target antibody (RBD-Ab), washing, binding of the detection antibody (DA-HRP), and the color reaction of the signal substrate are accomplished in order by shuttling the magnetic beads (Figure 1C). During visual signal acquisition, HRP on DA-HRP is combined with HCl for oxidizing TMB to the divalent state, and then etching AuNRs to generate different colors for semi-quantitative readout.[26,29]

https://doi.org/10.1021/acs.analchem.2c01260
Anal. Chem. 2022, 94, 8458−8465

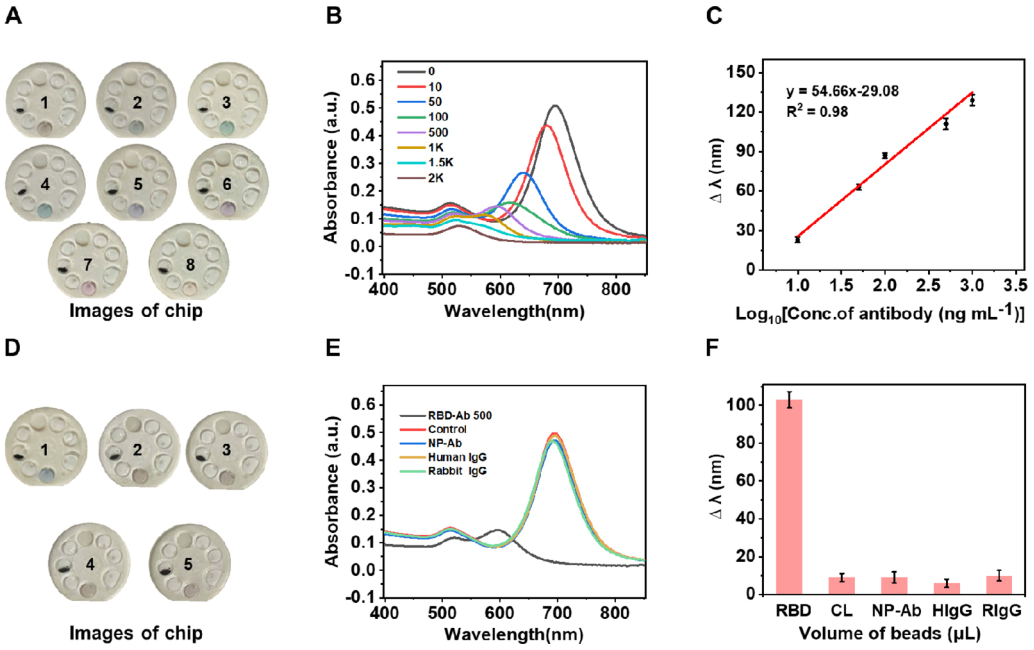

Figure 4. Assessment of the sensitivity and specificity of on-chip assay. (A) Visual analysis results at different RBD-Ab concentrations (0, 10, 50, 100, 500, 1000, 1500, and 2000 ng mL^{-1}). (B) Absorption spectra of AuNRs at different RBD-Ab concentrations. (C) Standard curve of $\triangle\lambda$ versus $\log_{10}$ [RBD-Ab]. (D) Visual analysis results for different proteins. (E) Absorption spectra of AuNRs with different proteins. (F) $\triangle\lambda$ of AuNRs for different proteins. The concentration of RBD-Ab is 500 ng mL^{-1}, and the concentrations of the other three proteins is 5000 ng mL^{-1}. The error bars represent mean value with standard deviation obtained from three replicates.

Preparation and Etching Optimization of Gold Nanorods. The morphology and etching condition of AuNRs are important factors that restrict the sensitivity of visual detection. AuNR solution is brown color when its absorbance (λ_{max}) is above 700 nm, while it will gradually show a variety of colors such as gray, blue, purple, or red when the λ_{max} is below 700 nm. Therefore, AuNRs with an initial λ_{max} of about 700 nm are very conducive to a high-performance color-changing analysis. As shown in Figure 2A−C, the TEM morphology characterization and elemental analysis results indicated a uniform size and high purity of AuNRs. In order to verify the etching principle of AuNRs, HRP, TMB, and HCl were used for etching AuNRs (Figure 2D). The λ_{max} value (703 nm) of the AuNRs did not show much shift under single reagent conditions, while a significant shift occurred when the three reagents participated cooperatively in the reaction. Hexadecyl trimethyl ammonium bromide (CTAB), as the solvent of AuNRs, aids in forming $AuBr_2^-$ during the etching of AuNRs.[26,29] As shown in Figure 2E, CTAB mediated the best etching effect when the concentration was 0.1 M. Since HCl can terminate the HRP enzymatic reaction and completely oxidize TMB, a sufficient dosage is necessary. When the HCl concentration was 1.0 M, the etching of AuNRs reached a plateau, indicating that the TMB in the system was completely oxidized (Figure 2F). Therefore, 1.0 M HCl was chosen to be the optimal concentration of HCl.

Verification of HRP Concentration-Dependent AuNR Etching. Since the concentration of target antibody can be evaluated by the concentration of HRP on the detection antibody (DA) by ELISA, the relationship between HRP and AuNR etching is important for sensitive analysis of antibody level. As shown in Figure 3A, during the reaction with a series of gradient concentrations of DA-HRP and 1.0 M HCl, TMB is oxidized and presents a yellow signal. Only by collecting the absorbance values with a microplate reader can the signal strength be distinguished. Instead, AuNRs can be etched by the generated TMB^{2+} from different concentrations of DA-HRP, resulting in varying degrees of peak shift (Figure 3B). Therefore, the detection results are converted from the original yellow signal of TMB to different color signals of AuNRs (Figure 3C), which can be easily distinguished by naked eye for semi-quantitative assessment of DA-HRP concentration. To further explore the reason for color change, TEM imaging of different experimental groups was performed to measure the size of the AuNRs. As shown in Figure 3D, as the concentration of DA-HRP increases, the AuNRs gradually change from a long rod shape to a spherical shape. With increased etching, the length of the AuNRs decreases significantly (Figure 3E), resulting in changes in the absorption spectra.

Fabrication and Manipulation of the Chip. The design of the four PMMA layers is shown in Figure S2A, including a bottom support layer, an aqueous phase layer containing reagent wells, an oil phase layer containing oil well, and the top layer with reagent inlets. The aqueous layer containing the reagent reservoirs is 3 mm thick, while the other three layers are 1 mm thick. After assembly and cleaning, the chip was successfully used for simulation experiments. As shown in Figure S2B, after reagent loading and oil sealing, with the help of the vertical and horizontal movement of the magnet, the magnetic beads can pass through the oil phase to participate in different reactions and mediated the visual analysis. Detailed operation can be found in Video 1 and Video 2.

Antibody Analysis in Buffer. Before on-chip experiments were undertaken, the experimental conditions of the ELISA system based on magnetic beads were optimized, including the concentration of skimmed milk in the blocking solution of magnetic beads or DA-HRP, the concentration of Tween-20 in the DA-HRP solution, and the number of magnetic beads used in one test (Figure S3). Briefly, PBS (0.05% Tween-20), containing 5% and 50% milk was used for DA-HRP dilution and magnetic bead dispersion, respectively, so that the lowest

https://doi.org/10.1021/acs.analchem.2c01260
Anal. Chem. 2022, 94, 8458−8465

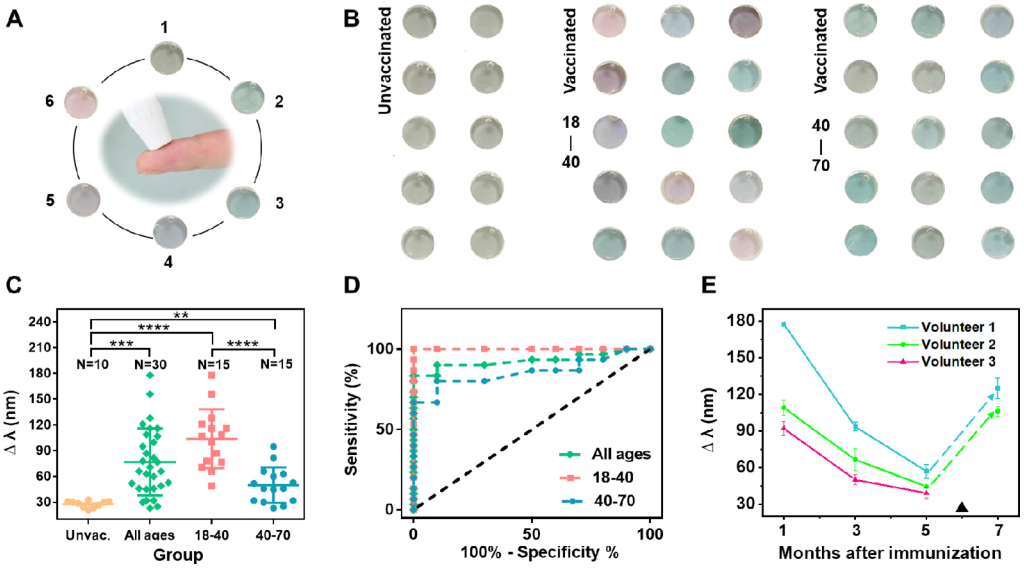

Figure 5. Antibody analysis in clinical samples. (A) Different colors (from number 1 to number 6) represent a gradual increase in antibody levels. (B) Antibody analysis of non-vaccine-immunized and vaccine-immunized volunteers. (C) $\triangle\lambda$ of AuNRs for nonimmunized and immunized volunteers. (D) ROC analysis of $\triangle\lambda$ between the nonimmunized and the immunized volunteer group. (E) Change in antibody levels in the body over time. Volunteers got booster vaccine at 6 months post-immunization. The smaller the $\triangle\lambda$ value, the lower the relative level of antibody.

background adsorption signal was realized. Then, the performance of on-chip analysis, mainly including sensitivity and specificity, were verified. The neutralizing antibody (RBD-Ab) with various concentrations of 0, 10, 50, 100, 500, 1000, 1500, and 2000 ng mL^{-1} was applied for analysis (Figure 4A). As a result, the corresponding AuNR colors were, in order, brown, gray, aquamarine, blue, purple, fuchsia, red, and pink. To obtain quantitative information, the solution was collected for absorbance measurement and $\triangle\lambda$ calculation (Figure 4B). $\triangle\lambda$ showed a good linear relationship in the antibody concentration range of 10−1000 ng mL^{-1} (Figure 4C). Then, RBD-Ab, PBS, NP-Ab, human IgG, and rabbit-IgG were adopted for specificity evaluation. As shown in Figure 4D, the experimental group with RBD-Ab was blue, while the results of other proteins all appeared brown or gray, similar to that of PBS. The absorption spectrum of each sample was also recorded for $\triangle\lambda$ calculation, showing that only the RBD-Ab experimental group has a significant $\triangle\lambda$ value (Figure 4E,F).

Clinical Sample Analysis. In order to evaluate the performance of the MMI-Chip in clinical applications, samples from 10 non-vaccine-immunized volunteers and 30 vaccine-immunized volunteers were used for the analysis of RBD-Ab. The relative level of antibody can be estimated by the final color of the AuNRs. Gray, aquamarine, blue, purple, fuchsia, and red represent a gradual increase in antibody levels (Figure 5A). As shown in Figure 5B, all 10 non-vaccine-immunized sera generated gray signals, indicating low concentrations of RBD-Ab. In contrast, different colors were observed among 30 vaccine-immunized sera from volunteers of different ages, indicating the different levels of RBD-Ab. The clinical sensitivity of the method were calculated according to Table S3.[28] With the gray hole as a control, the sensitivity for different sample groups (all ages, 18−40, 40−70) were (15 + 10)/30 = 83.3%, 15/15 = 100%, and 10/15 = 66.6%, respectively.

To further digitize the difference in antibody levels between different individuals, the AuNRs solutions were re-collected for absorbance measurement and $\triangle\lambda$ calculation. As shown in Figure 5C, $\triangle\lambda$ of vaccine-immunized sera is significantly higher than that of non-vaccine-immunized sera. Additionally, the $\triangle\lambda$ derived from individuals of 18−40 years old are significantly higher than that of individuals over 40 years old. From the ROC curve in Figure 5D, the corresponding AUC values (the area under the curve and the coordinate axis) of different age groups (all ages, 18−40, 40−70) are 0.928, 1.000, and 0.857, respectively, representing reliable analytical results. Overall, based on the color differences and digitized results, it can be concluded that older individuals (aged 40−70) showed relatively weaker immune responses compared to younger volunteers (aged 18−40). Additionally, no significant difference was observed in $\triangle\lambda$ between genders (Figure S4A). Detailed volunteer information is presented in Tables S1 and S2. It is worth noting that high antibody levels indicate that the body has a better immune response, which is suitable for qualitative assessment of antiviral effect. However, there was no direct quantitative relationship between the antibody level and virus neutralization capacity, which is restricted by detection standards, virus mutations, and so on.[4] Furthermore, to assess the reliability, the results of the MMI-Chip were compared with those generated by the traditional ELISA method (Figure S4B). As shown in Figure S4C,D, there was a linear consistent result (R^2 = 0.9018) and an average bias of 1.9 ng mL^{-1} from −33.0 to −36.8 ng mL^{-1} with 95% confidence interval, indicating that the MMI-Chip assay is feasible for antibody assay in clinical samples. Additionally, antibody analysis can be performed with a simple fingertip blood draw, thanks to the small sample volume required for the experiment. We compared the antibody levels of venous blood and fingertip blood of the same volunteer. As shown in Figure S5, there was no significant difference in antibody levels.

The analysis of antibody levels at different time points after immunization is helpful not only for identifying people with relatively low immune responses but also for finding the best vaccine booster immunity time. In this work, we conducted a follow-up analysis based on NAbs levels on vaccine-immunized volunteers. As shown in Figure 5E, as time goes by, $\triangle\lambda$ gradually decreases, indicating a decrease of NAbs. The

https://doi.org/10.1021/acs.analchem.2c01260
Anal. Chem. 2022, 94, 8458−8465

antibody level decreased to half the initial value at about 3 months and reached a relatively low level at 5 months. Similarly, some studies have shown that the half-life of anti-SARS-CoV-2 RBD IgG antibodies in individuals following viral infection was found to be ~110 days.[30,31] To maintain individual's dynamic antibody levels for a better protection against SARS-CoV-2, the booster immunization of vaccine is scheduled for 5−6 months in most countries. It can be seen from the Figure 5E that the antibody level of the volunteers rebounded significantly after 1 month of booster immunization.

CONCLUSIONS

In summary, we have constructed a novel magnetofluid-integrated multicolor immunochip (MMI-Chip) for visual analysis of neutralizing antibodies to SARS-CoV-2 variants. The three-dimensional oil−water two-phase structure of the chip enables multistep reactions to be integrated into a simple, closed magnetofluid immunoassay system. By using the chip, external exposure caused by multistep reagent addition can be avoided so as to achieve biological safety and user-friendliness. Additionally, compared to the traditional oil−water two-dimensional structure, the three-dimensional structure allows mixing and addition of reagents, benefiting from the variable volume of the upper oil phase. In the analysis of clinical samples, the MMI-Chip realized the identification of vaccine-immunized volunteers with a sensitivity of 83.3%, and the results were linearly correlated with that of the standard ELISA method. Furthermore, through the visual multicolor signals, the antibody level of the same immunized individual can also be monitored over time. In short, the MMI-Chip platform represents a new and rapid detection strategy for determination of antibody concentration, and will inspire further study of integrated microfluidic analytical systems.

ASSOCIATED CONTENT

Supporting Information

The Supporting Information is available free of charge at https://pubs.acs.org/doi/10.1021/acs.analchem.2c01260.

Design of the microfluidic chip by Auto-CAD software; working diagram of the MMI-Chip; optimization of the ELISA system; analysis of clinical samples; analysis of antibody levels in fingertip blood and venous blood; detailed information for volunteers; and calculation of sensitivity and specificity for clinical diagnosis (Figures S1−S5 and Tables S1−S3) (PDF)

Detailed operation of fabrication and manipulation of the chip (MP4) (MP4)

AUTHOR INFORMATION

Corresponding Author

Zhi Zhu − *MOE Key Laboratory of Spectrochemical Analysis & Instrumentation, Collaborative Innovation Center of Chemistry for Energy Materials, Key Laboratory for Chemical Biology of Fujian Province, State Key Laboratory of Physical Chemistry of Solid Surfaces, Department of Chemical Biology, College of Chemistry and Chemical Engineering, Xiamen University, Xiamen 361005, China*; orcid.org/0000-0002-3287-4920; Phone: + 86-592-2187601; Email: zhuzhi@xmu.edu.cn

Authors

Haicong Shen − *MOE Key Laboratory of Spectrochemical Analysis & Instrumentation, Collaborative Innovation Center of Chemistry for Energy Materials, Key Laboratory for Chemical Biology of Fujian Province, State Key Laboratory of Physical Chemistry of Solid Surfaces, Department of Chemical Biology, College of Chemistry and Chemical Engineering, Xiamen University, Xiamen 361005, China*

Xinying Chen − *Clinical Laboratory, Xiamen University Hospital, Xiamen 361005, China*

Liuqing Zeng − *MOE Key Laboratory of Spectrochemical Analysis & Instrumentation, Collaborative Innovation Center of Chemistry for Energy Materials, Key Laboratory for Chemical Biology of Fujian Province, State Key Laboratory of Physical Chemistry of Solid Surfaces, Department of Chemical Biology, College of Chemistry and Chemical Engineering, Xiamen University, Xiamen 361005, China*

Xing Xu − *MOE Key Laboratory of Spectrochemical Analysis & Instrumentation, Collaborative Innovation Center of Chemistry for Energy Materials, Key Laboratory for Chemical Biology of Fujian Province, State Key Laboratory of Physical Chemistry of Solid Surfaces, Department of Chemical Biology, College of Chemistry and Chemical Engineering, Xiamen University, Xiamen 361005, China*

Yingzhou Tao − *MOE Key Laboratory of Spectrochemical Analysis & Instrumentation, Collaborative Innovation Center of Chemistry for Energy Materials, Key Laboratory for Chemical Biology of Fujian Province, State Key Laboratory of Physical Chemistry of Solid Surfaces, Department of Chemical Biology, College of Chemistry and Chemical Engineering, Xiamen University, Xiamen 361005, China*

Siyin Kang − *MOE Key Laboratory of Spectrochemical Analysis & Instrumentation, Collaborative Innovation Center of Chemistry for Energy Materials, Key Laboratory for Chemical Biology of Fujian Province, State Key Laboratory of Physical Chemistry of Solid Surfaces, Department of Chemical Biology, College of Chemistry and Chemical Engineering, Xiamen University, Xiamen 361005, China*

Yinzhu Lu − *MOE Key Laboratory of Spectrochemical Analysis & Instrumentation, Collaborative Innovation Center of Chemistry for Energy Materials, Key Laboratory for Chemical Biology of Fujian Province, State Key Laboratory of Physical Chemistry of Solid Surfaces, Department of Chemical Biology, College of Chemistry and Chemical Engineering, Xiamen University, Xiamen 361005, China*

Mingjian Lian − *Clinical Laboratory, The First Affiliated Hospital of Xiamen University, Xiamen 361005, China*

Chaoyong Yang − *MOE Key Laboratory of Spectrochemical Analysis & Instrumentation, Collaborative Innovation Center of Chemistry for Energy Materials, Key Laboratory for Chemical Biology of Fujian Province, State Key Laboratory of Physical Chemistry of Solid Surfaces, Department of Chemical Biology, College of Chemistry and Chemical Engineering, Xiamen University, Xiamen 361005, China; Institute of Molecular Medicine, Department of Gastrointestinal Surgery, Renji Hospital, School of Medicine, Shanghai Jiao Tong University Shanghai, Shanghai 200127, China*; orcid.org/0000-0002-2374-5342

Complete contact information is available at: https://pubs.acs.org/10.1021/acs.analchem.2c01260

https://doi.org/10.1021/acs.analchem.2c01260
Anal. Chem. 2022, 94, 8458−8465

Author Contributions

All authors have given approval to the final version of the manuscript.

Notes

The authors declare no competing financial interest.

■ ACKNOWLEDGMENTS

We thank the National Natural Science Foundation of China (21974113, 21775128, and 21735004), National Key R&D Program of China (2021YFA0909400), Program for Chang Jiang Scholars and Innovative Research Teams in University (IRT13036), Medical and Health Program of Xiamen (3502Z20189005), and the National Science Fund for Fostering Talents in Basic Science (NFFTBS, J1310024) for their financial support.

■ REFERENCES

(1) Zheng, J. *Int. J. Biol. Sci.* **2020**, *16*, 1678−1685.
(2) Lippi, G.; Sanchis-Gomar, F.; Henry, B. M. *Ann. Transl. Med.* **2020**, *8*, 693.
(3) Deepak, P.; Kim, W.; Paley, M. A.; Yang, M.; Carvidi, A. B.; el-Qunni, A. A.; Haile, A.; Huang, K.; Kinnett, B.; Liebeskind, M. J.; Liu, Z.; McMorrow, L. E.; Paez, D.; Perantie, D. C.; Schriefer, R. E.; Sides, S. E.; Thapa, M.; Gergely, M.; Abushamma, S.; Klebert, M.; Mitchell, L.; Nix, D.; Graf, J.; Taylor, K. E.; Chahin, S.; Ciorba, M. A.; Katz, P.; Matloubian, M.; O'Halloran, J. A.; Presti, R. M.; Wu, G. F.; Whelan, S. P. J.; Buchser, W. J.; Gensler, L. S.; Nakamura, M. C.; Ellebedy, A. H.; Kim, A. H. J. *medRxiv* **2021**, No. 21254656.
(4) Lippi, G.; Henry, B. M.; Plebani, M. *Diagnostics (Basel)* **2021**, *11*, 941.
(5) Jackson, C. B.; Farzan, M.; Chen, B.; Choe, H. *Nat. Rev. Mol. Cell Biol.* **2022**, *23*, 3−20.
(6) Ju, B.; Zhang, Q.; Ge, J.; Wang, R.; Sun, J.; Ge, X.; Yu, J.; Shan, S.; Zhou, B.; Song, S.; Tang, X.; Yu, J.; Lan, J.; Yuan, J.; Wang, H.; Zhao, J.; Zhang, S.; Wang, Y.; Shi, X.; Liu, L.; Zhao, J.; Wang, X.; Zhang, Z.; Zhang, L. *Nature* **2020**, *584*, 115−119.
(7) Wang, J. J.; Zhang, N.; Richardson, S. A.; Wu, J. V. *Expert Rev. Mol. Diagn.* **2021**, *21*, 363−370.
(8) Piccoli, L.; Park, Y.-J.; Tortorici, M. A.; Czudnochowski, N.; Walls, A. C.; Beltramello, M.; Silacci-Fregni, C.; Pinto, D.; Rosen, L. E.; Bowen, J. E.; Acton, O. J.; Jaconi, S.; Guarino, B.; Minola, A.; Zatta, F.; Sprugasci, N.; Bassi, J.; Peter, A.; De Marco, A.; Nix, J. C.; Mele, F.; Jovic, S.; Rodriguez, B. F.; Gupta, S. V.; Jin, F.; Piumatti, G.; Lo Presti, G.; Pellanda, A. F.; Biggiogero, M.; Tarkowski, M.; Pizzuto, M. S.; Cameroni, E.; Havenar-Daughton, C.; Smithey, M.; Hong, D.; Lepori, V.; Albanese, E.; Ceschi, A.; Bernasconi, E.; Elzi, L.; Ferrari, P.; Garzoni, C.; Riva, A.; Snell, G.; Sallusto, F.; Fink, K.; Virgin, H. W.; Lanzavecchia, A.; Corti, D.; Veesler, D. *Cell* **2020**, *183*, 1024−1042.e21.
(9) Baer, A.; Kehn-Hall, K. *J. Vis. Exp.* **2014**, No. e52065.
(10) Vickers, M. A.; Sariol, A.; Leon, J.; Ehlers, A.; Locher, A. V.; Dubay, K. A.; Collins, L.; Voss, D.; Odle, A. E.; Holida, M.; Merrill, A. E.; Perlman, S.; Knudson, C. M. *Transfusion* **2021**, *61*, 2099−2106.
(11) Shi, A. C.; Ren, P. *J. Immunol. Methods* **2021**, *494*, No. 113060.
(12) Lippi, G.; Henry, B. M.; Plebani, M. *J. Lab. Precis. Med.* **2021**, *6*, 2519−9005.
(13) Cameron, A.; Porterfield, C. A.; Byron, L. D.; Wang, J.; Pearson, Z.; Bohrhunter, J. L.; Cardillo, A. B.; Ryan-Muntz, L.; Sorensen, R. A.; Caserta, M. T.; Angeloni, S.; Hardy, D. J.; Zand, M. S.; Pecora, N. D.; Tang, Y.-W. *medrxiv* **2021**, *59*, e02489−e02420.
(14) Wang, H.; Li, X.; Li, T.; Wang, L.; Wang, L.; Lin, J.; Zhang, S.; Xu, Y.; Wei, W. *Clin. Respir. J.* **2021**, *15*, 499−505.
(15) Wang, C.; Liu, M.; Wang, Z. F.; Li, S.; Deng, Y.; He, N. Y. *Nano Today* **2021**, *37*, No. 101092.
(16) Gervais, L.; de Rooij, N.; Delamarche, E. *Adv. Mater.* **2011**, *23*, H151−H176.
(17) Nasseri, B.; Soleimani, N.; Rabiee, N.; Kalbasi, A.; Karimi, M.; Hamblin, M. R. *Biosens. Bioelectron.* **2018**, *117*, 112−128.
(18) Juang, D. S.; Juang, T. D.; Dudley, D. M.; Newman, C. M.; Accola, M. A.; Rehrauer, W. M.; Friedrich, T. C.; O'Connor, D. H.; Beebe, D. J. *Nat. Commun.* **2021**, *12*, 4317.
(19) Trick, A. Y.; Melendez, J. H.; Chen, F.-E.; Chen, L.; Onzia, A.; Zawedde, A.; Nakku-Joloba, E.; Kyambadde, P.; Mande, E.; Matovu, J.; Atuheirwe, M.; Kwizera, R.; Gilliams, E. A.; Hsieh, Y.-H.; Gaydos, C. A.; Manabe, Y. C.; Hamill, M. M.; Wang, T.-H. *Sci. Transl. Med.* **2021**, *13*, No. eabf6356.
(20) Qu, J.; Chenier, M.; Zhang, Y.; Xu, C.-Q. *Micromachines* **2021**, *12*, 433.
(21) Song, Y. J.; Wang, Y. Z.; Qi, W. J.; Li, Y.; Xuan, J.; Wang, P.; Qin, L. D. *Lab Chip* **2016**, *16*, 2955−2962.
(22) Yang, Y.; Zeng, Y. *Lab Chip* **2018**, *18*, 3830−3839.
(23) Tian, F.; Liu, C.; Deng, J.; Han, Z.; Zhang, L.; Chen, Q.; Sun, J. *Sci. China Chem.* **2020**, *63*, 1498−1506.
(24) Abate, M. F.; Ahmed, M. G.; Li, X. R.; Yang, C. Y.; Zhu, Z. *Lab Chip* **2020**, *20*, 3625−3632.
(25) Liu, D.; Zhang, Y.; Zhu, M.; Yu, Z.; Ma, X.; Song, Y.; Zhou, S.; Yang, C. *Anal. Chem.* **2020**, *92*, 11826−11833.
(26) Ma, X.; Lin, Y.; Guo, L.; Qiu, B.; Chen, G.; Yang, H.-H.; Lin, Z. *Biosens. Bioelectron.* **2017**, *87*, 122−128.
(27) Ye, X. C.; Zheng, C.; Chen, J.; Gao, Y. Z.; Murray, C. B. *Nano Lett.* **2013**, *13*, 765−771.
(28) Shen, H.; Su, R.; Peng, J.; Zhu, L.; Deng, K.; Niu, Q.; Song, Y.; Yang, L.; Wu, L.; Zhu, Z.; Yang, C. *Bioact. Mater.* **2022**, *11*, 32−40.
(29) Chen, Z.; Chen, C.; Huang, H.; Luo, F.; Guo, L.; Zhang, L.; Lin, Z.; Chen, G. *Anal. Chem.* **2018**, *90*, 6222−6228.
(30) Doria-Rose, N.; Suthar, M. S.; Makowski, M.; O'Connell, S.; McDermott, A. B.; Flach, B.; Ledgerwood, J. E.; Mascola, J. R.; Graham, B. S.; Lin, B. C.; O'Dell, S.; Schmidt, S. D.; Widge, A. T.; Edara, V.-V.; Anderson, E. J.; Lai, L.; Floyd, K.; Rouphael, N. G.; Zarnitsyna, V.; Roberts, P. C.; Makhene, M.; Buchanan, W.; Luke, C. J.; Beigel, J. H.; Jackson, L. A.; Neuzil, K. M.; Bennett, H.; Leav, B.; Albert, J.; Kunwar, P.; mRNA-1273 Study Group. *N. Engl. J. Med. Overseas Ed.* **2021**, *384*, 2259−2261.
(31) Iyer, A. S.; Jones, F. K.; Nodoushani, A.; Kelly, M.; Becker, M.; Slater, D.; Mills, R.; Teng, E.; Kamruzzaman, M.; Garcia-Beltran, W. F.; Astudillo, M.; Yang, D.; Miller, T. E.; Oliver, E.; Fischinger, S.; Atyeo, C.; Iafrate, A. J.; Calderwood, S. B.; Lauer, S. A.; Yu, J.; Li, Z.; Feldman, J.; Hauser, B. M.; Caradonna, T. M.; Branda, J. A.; Turbett, S. E.; LaRocque, R. C.; Mellon, G.; Barouch, D. H.; Schmidt, A. G.; Azman, A. S.; Alter, G.; Ryan, E. T.; Harris, J. B.; Charles, R. C. *Sci. Immunol.* **2020**, *5*, No. eabe0367.

https://doi.org/10.1021/acs.analchem.2c01260
Anal. Chem. 2022, 94, 8458−8465